Topographically Induced Dispersion in a Salt Marsh Estuary

ADRIAN MIKHAIL P. GARCIA,[a,b] TONG BO,[b,c] W. ROCKWELL GEYER,[b] AND DAVID K. RALSTON[b]

[a] *Exponent, Inc., Bellevue, Washington*
[b] *Applied Ocean Physics and Engineering, Woods Hole Oceanographic Institution, Woods Hole, Massachusetts*
[c] *Department of Mechanics and Engineering Science, College of Engineering, Peking University, Beijing, China*

(Manuscript received 30 December 2024, in final form 21 June 2025, accepted 25 August 2025)

ABSTRACT: The salt balance in estuaries is maintained by the outflow from the river, which removes salt from the estuary, and dispersive processes, which drive downgradient fluxes bringing salt into the estuary. We analyzed the salt fluxes in a realistic model of the North River, a tidal salt marsh estuary, using a quasi-Lagrangian moving plane reference based on the theory of Dronkers and van de Kreeke. Our study confirms their theoretical finding that in a plane moving with the tides, all landward salt flux results directly from shear dispersion, that is, the spatial correlation between cross-sectional variations in velocity and salinity. We separated cross-sectional variations in velocity and salinity not only based on their lateral and vertical components but also by distinct regions of the cross section: the main channel and the marsh. In this way, we quantified the salt flux contributions from vertical and lateral shear dispersion, as well as from trapping—the salt flux due to the difference between the mean velocity and salinity of the main channel compared to the marsh. Trapping accounted for up to half of the total landward salt flux in the estuary during spring tides but decreased to about one-quarter during neap tides. Within the channel, the primary mode of dispersion shifted from lateral shear dispersion due to flow separation during spring tides to vertical shear dispersion due to tidal straining during neap tides. These results demonstrate the important role of topographically induced dispersion on maintaining the salt balance, particularly in tidally dominated estuaries.

KEYWORDS: Estuaries; Coastal flows; Dispersion; Mass fluxes/transport; Topographic effects; Tides

1. Introduction

The salinity intrusion in an estuary depends on the balance between the seaward salt flux due to advection by the river outflow and the landward salt flux resulting from estuarine and tidal processes (Pritchard 1952; Fischer 1972). For long estuaries in which the salinity intrusion length is much greater than the tidal excursion, the landward salt flux is driven primarily by the estuarine circulation (Hansen and Rattray 1965; Chatwin 1976; Chen et al. 2012), a steady (i.e., tidally averaged) baroclinic exchange flow that is seaward at the surface and landward at depth. However, for short estuaries in which the salinity intrusion length is similar to the tidal excursion, the landward salt flux is driven primarily by tidal dispersion (Hughes and Rattray 1980; Chen et al. 2012), the net downgradient transport of scalars caused by oscillatory and spatially varying tidal currents.

Topography plays an important role in enhancing tidal dispersion in estuaries (Zimmerman 1986; Geyer and Signell 1992). Various mechanisms of topographically induced tidal dispersion include jet–sink exchange at a constriction (Stommel and Farmer 1952; Chen et al. 2012), lateral trapping in shoals and side channels (Schijf and Schonfeld 1953; Okubo 1973), and tidal eddies due to flow separation past headlands (Geyer and Signell 1992). Through each of these processes, the presence of topographic variations leads to large spatial variations in the local velocity field, thereby enhancing along-channel transport by shear dispersion (Taylor 1953, 1954).

At a fixed location in an estuary, the landward salt flux is the result of both spatial correlations between the cross-sectional varying components of velocity and salinity over a cross section as well as temporal correlations between the cross-section averaged velocity and salinity over a tidal cycle (Fischer et al. 1979; Hughes and Rattray 1980). Mechanisms of shear dispersion can be readily tied to the local velocity and salinity structure that produce the spatial correlation salt flux. However, the physics by which the cross-section averaged velocity and salinity are shifted out of quadrature to produce the temporal correlation salt flux in an Eulerian reference frame is not as evident.

Dronkers and van de Kreeke (1986) provided a theoretical analysis of the temporal correlation term by considering the salt flux through a moving plane that follows the motion of the tides. In this quasi-Lagrangian reference frame, the cross-sectionally averaged tidal transport vanishes by definition, and therefore, the temporal correlation salt flux becomes zero. Thus, all landward salt flux through the moving plane is due only to the spatial correlation term. By equating the salt fluxes in the moving plane to the salt fluxes at a fixed cross section having the same tidally averaged salinity, they demonstrated that the temporal correlation salt flux through the fixed cross section is equal to the difference between the spatial correlation salt flux in the moving plane and spatial correlation salt flux at the fixed cross section. Therefore, they referred to the temporal correlation salt flux as "nonlocal" dispersion because it represents shear dispersion that happens elsewhere in the estuary within a tidal excursion, whereas they referred to the spatial correlation salt flux as "local" dispersion because it represents shear dispersion which occurs at that cross section.

Applying the moving plane framework of Dronkers and van de Kreeke (1986) in an idealized numerical modeling

---

Corresponding author: Adrian Mikhail P. Garcia, garciaa@exponent.com

DOI: 10.1175/JPO-D-24-0261.1

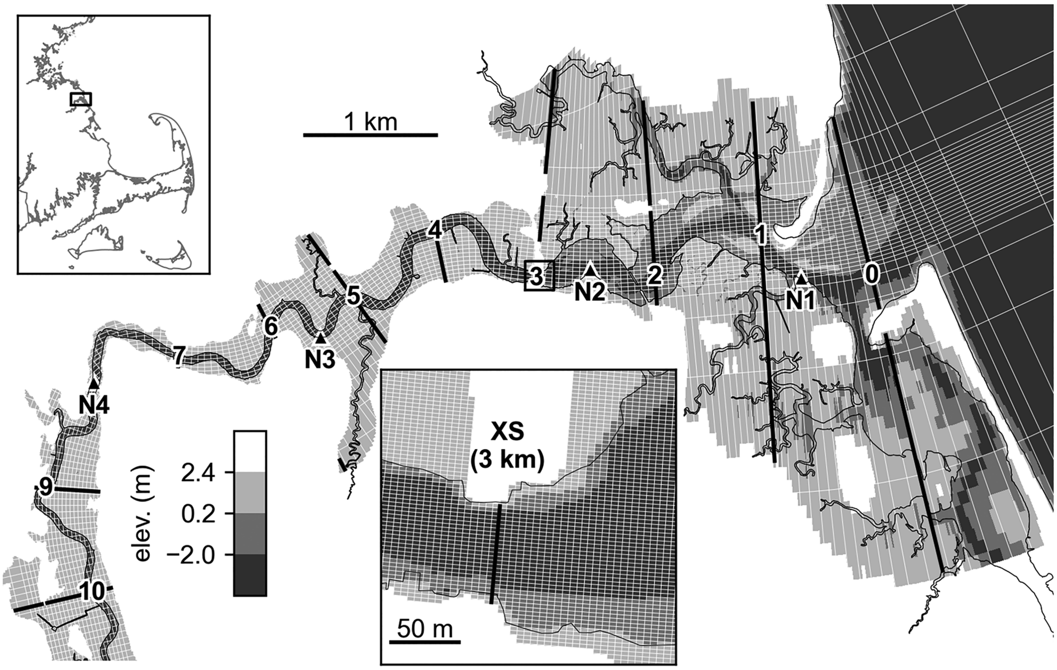

FIG. 1. Map and bathymetry of the North River estuary. Moorings from the 2021 field observations are labeled by the black triangles. Along-channel location is labeled at every 1 km with the model transects over which salt fluxes are calculated shown by the thick black lines. The model grid is plotted at every tenth point in white. The location of the cross section (XS) at 3 km, located at a bridge constriction, is highlighted by the black box and shown with a zoomed-in view, where the model grid is plotted at every single point in white. The map inset at the top left shows the location of the North River on the New England shelf.

study of a short estuary, Garcia and Geyer (2023) confirmed that all landward salt flux is the result of shear dispersion somewhere within the estuary or adjacent coastal waters. Using the quasi-Lagrangian reference frame, they demonstrated how the locally enhanced shear dispersion in regions of topographic variation (e.g., the mouth, channel constrictions, bends) provided the primary source of the landward salt flux throughout the estuary. Furthermore, their results highlighted the spatiotemporal variability of shear dispersion in short, tidally dominated systems, for which the moving plane framework must be applied to explain the large temporal correlation salt fluxes, i.e., the nonlocal contributions to the landward salt flux.

This study builds on the results of Garcia and Geyer (2023) by applying the quasi-Lagrangian moving plane analysis of Dronkers and van de Kreeke (1986) to model simulations using a realistic configuration of the North River, a tidal salt marsh estuary, to investigate the influence of complex topography on dispersive processes. To our knowledge, this is the first study to apply the moving plane analysis to realistic model simulations. Section 2 describes the field site, observations, and numerical model. Additionally, section 2 provides an overview of the estuarine salt balance and analysis of the landward salt flux using both the traditional Eulerian salt flux decomposition as well as the quasi-Lagrangian approach of Dronkers and van de Kreeke (1986). A framework is presented for separating the spatial correlation salt flux not only into its contributions from lateral and vertical shear dispersion within the channel but also from the trapping of water on the marsh at high tide (HT) and in lateral side channels. In section 3, the Eulerian salt flux through a fixed cross section is compared with the salt flux through the corresponding moving plane. Then, the tidally varying position of the moving plane is used to identify the mechanisms that contribute most strongly to the landward salt flux under spring and neap tidal conditions. Section 4 discusses the primary modes of dispersion throughout the estuary under different forcing conditions and compares the moving plane analysis to both the traditional Eulerian approach and total exchange flow (MacCready 2011) methods for evaluating the salt flux. A summary of conclusions is presented in section 5.

2. Methods

a. Site description

The North River is a tidal salt marsh estuary located in Marshfield, Massachusetts (MA) (Fig. 1). The estuary varies from well-mixed to stratified conditions depending on the forcing conditions (Kranenburg et al. 2019; Garcia et al. 2022; Bo et al. 2021). The river flow in the North River varies seasonally, with typical peak daily values reaching up to 30 $m^3\ s^{-1}$ during the spring season and low monthly averages of about 0.5 $m^3\ s^{-1}$ during the summer. Tides are semidiurnal, and the tidal range near the mouth varies from 2 to 3.5 m over the spring–neap cycle. With the exception of the regions near topographic features (e.g., constrictions) where currents can exceed 1 $m\ s^{-1}$,

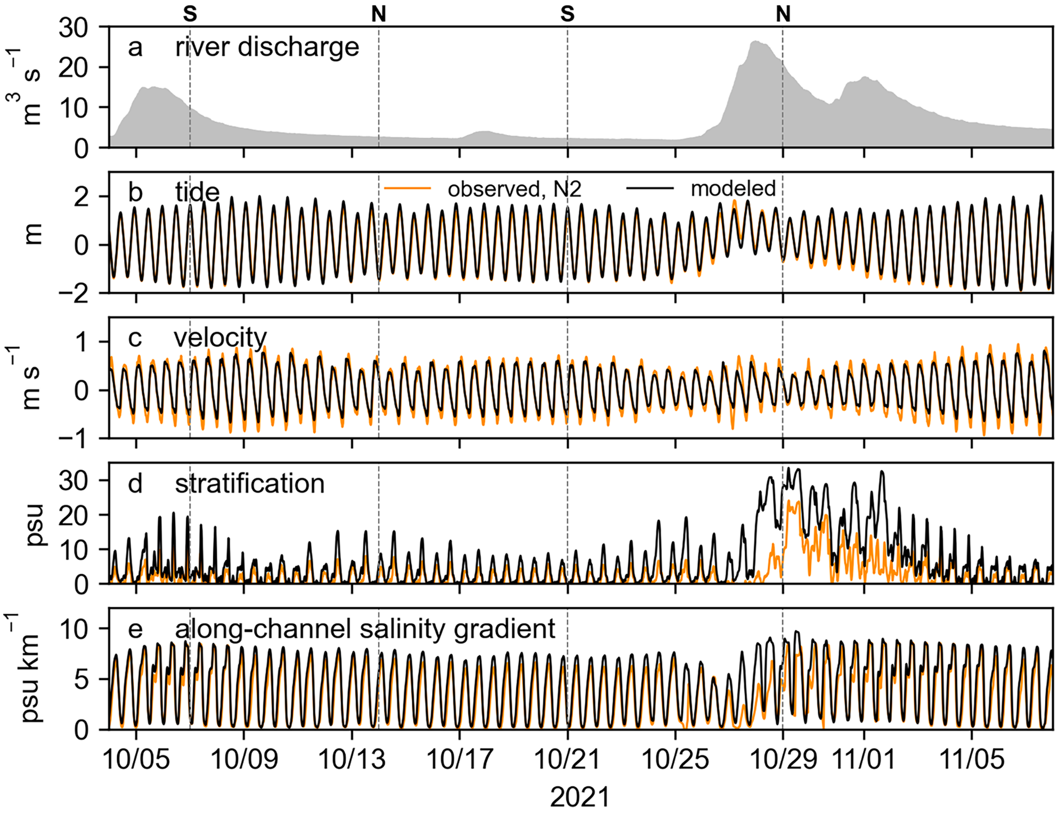

FIG. 2. Time series of estuary conditions at the N2 mooring during the period of observations in 2021. (a) River discharge from a USGS gauge (01105730) scaled by a factor of 2.3 to account for the additional catchment area below the gauge. (b) Tidal water level. (c) Depth-averaged streamwise velocity. (d) Top–bottom salinity stratification. (e) Along-channel salinity gradient estimated from bottom salinity at the N1 and N3 moorings. In (b)–(e), the orange lines are from observations and the black lines are from the model. The vertical dotted lines indicate the time periods shown in Figs. 6 and 15.

the cross-section averaged tidal velocity amplitudes in the channel typically range from 0.3 to 0.5 m s^{-1}, corresponding to tidal excursion distances of 3–7 km. The along-channel salinity gradient at the middle of the estuary ranges about 6–8 psu km^{-1}, corresponding to estuarine length scales of about 4–6 km. Based on the tidal excursion distance being comparable to the length of the salinity intrusion, the North River would be classified as a “short” estuary (Chen et al. 2012).

The main channel of the North River is joined by multiple smaller tributaries along its length and intersects with the South River near the mouth, where the estuary system connects to the Atlantic Ocean through Massachusetts Bay. In the region within 3 km from the mouth, the estuary has intertidal shoals spanning up to 1 km in width and about 1 m deep at mean water level, whereas the main channel is typically 60–100 m wide and 4–6 m deep along its thalweg throughout the study site. The wide intertidal shoal region of the estuary is separated from the narrow upper-channel region by a bridge crossing located 3 km from the mouth (see Fig. 1). Another sharp channel constriction is located 2 km from the mouth where the width of the main channel is reduced from 100 to 40 m and the depth increases to nearly 10 m. Throughout the estuary system, the channels are surrounded by wide intertidal salt marshes at an elevation of about 1 m above mean water level.

b. *Numerical model*

The Regional Ocean Modeling System (ROMS) was used to simulate the North River estuary. ROMS is a 3D hydrostatic structured-grid model based on the Reynolds-averaged Navier–Stokes (RANS) equations (Shchepetkin and McWilliams 2005; Haidvogel et al. 2008; Warner et al. 2005a). The model domain extends 7 km offshore from the coastline and 20 km inside the estuary (Fig. 1). An orthogonal curvilinear grid was built to follow the general direction of the marsh platform inside the estuary and was aligned with the orientation of the coastline outside the estuary. The highest resolution is 3 m in the channel (around 10–30 grid cells across the channel), and grid spacing increases in the ocean and over the marsh away from the channel. In the vertical direction, 16 uniformly distributed layers were used.

The model has tidal and subtidal forcings on the open ocean boundary (east side of the model domain) with Chapman (1985) and Flather (1976) boundary conditions for the free surface and depth-averaged velocity, respectively. Tidal constituents

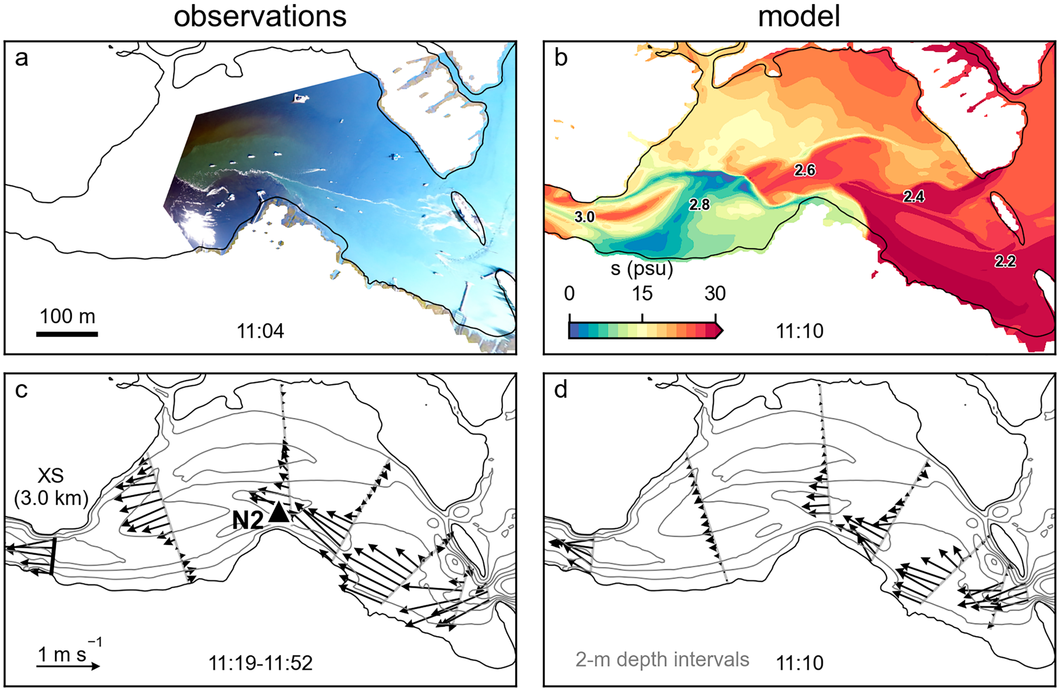

FIG. 3. Tidal intrusion front and lateral flow separation during flood tide on 7 Oct. (a) Aerial drone imagery depicting light blue-green water separated from darker blue water by a sharp front, indicated by the white surface foam lines. The white area in the southwest region of the image is reflection from the sun. (b) Surface salinity from the model output, with channel markers at 200-m intervals. (c) Surface velocity vectors from shipboard ADCP surveys. (d) Surface velocity vectors from model. In (c) and (d), the bathymetry is shown in gray at 2-m contour intervals.

were extracted from the advanced circulation (ADCIRC) database (Luettich et al. 1992), while subtidal fluctuations were obtained from the low-pass-filtered water surface elevation record from the National Oceanic and Atmospheric Administration (NOAA) station at Boston (8443970). River discharge was input from the west side of the model domain with data from the USGS gauge at Hanover (01105730) multiplied by 2.3 to account for the additional catchment area of the North River downstream from the gauging station. No freshwater sources were added at the heads of the tributaries joining the main channel of the North River. However, with the exception of the two largest channels that join the North River near the mouth of the estuary, the combined catchment areas of all other tributaries account for less than 10% of the total North River watershed. Therefore, we expect the exclusion of additional freshwater sources to have little impact on the salinity structure in the estuarine region of the North River, though this may affect the region near the mouth.

The k–ϵ implementation of the generic length scale (GLS) formulation for turbulence closure was used for vertical mixing (Umlauf and Burchard 2003; Warner et al. 2005b). The bottom roughness z_0 was a uniform 0.005 m throughout the domain, except near the along-channel location 7 km where z_0 was locally increased to up to 0.2 m to represent rocks on the bed. A third-order upwind advection scheme was used for horizontal advection. The horizontal mixing coefficient was set as 0.01 m^2 s^{-1}. An algorithm for wetting and drying (Warner et al. 2013) was enabled with a small critical depth of 0.02 m to simulate the tidal inundation and drainage processes over the marsh platform and shallow areas of the channel.

The model setup, calibration, and initial skill evaluation were presented by Bo et al. (2023), who validated the model setup using observations from field studies in 2017 (Kranenburg et al. 2019; Bo et al. 2021). An additional skill evaluation was presented by Bo et al. (2024) (see supplemental information), who further validated the model setup using observations from a different field study in 2021 (Garcia 2022). In this paper, we focus on the simulation and observation period from 2021.

c. *Observations*

During the fall of 2021, a 49-day field campaign including time series measurements, shipboard surveys, and aerial drone imagery was conducted in the North River (Garcia 2022; Bo et al. 2024). Over the period of measurements, the river discharge ranged from 2 to 25 m^3 s^{-1} (Fig. 2a), which was relatively high for the early fall season due to the wet summer which preceded it. Strong spring tides occurred during early October and early November, with neap tides occurring in late October. The large sea level setup of 0.8 m and peak flow conditions on 27 October corresponded to a tropical cyclone (Tropical Storm Wanda).

Time series measurements of salinity, velocity, and tides were obtained at moorings spaced at 2–3-km intervals along the main channel of the estuary (see Fig. 1) with surface and bottom conductivity–temperature–depth (CTD) sensors (RBR)

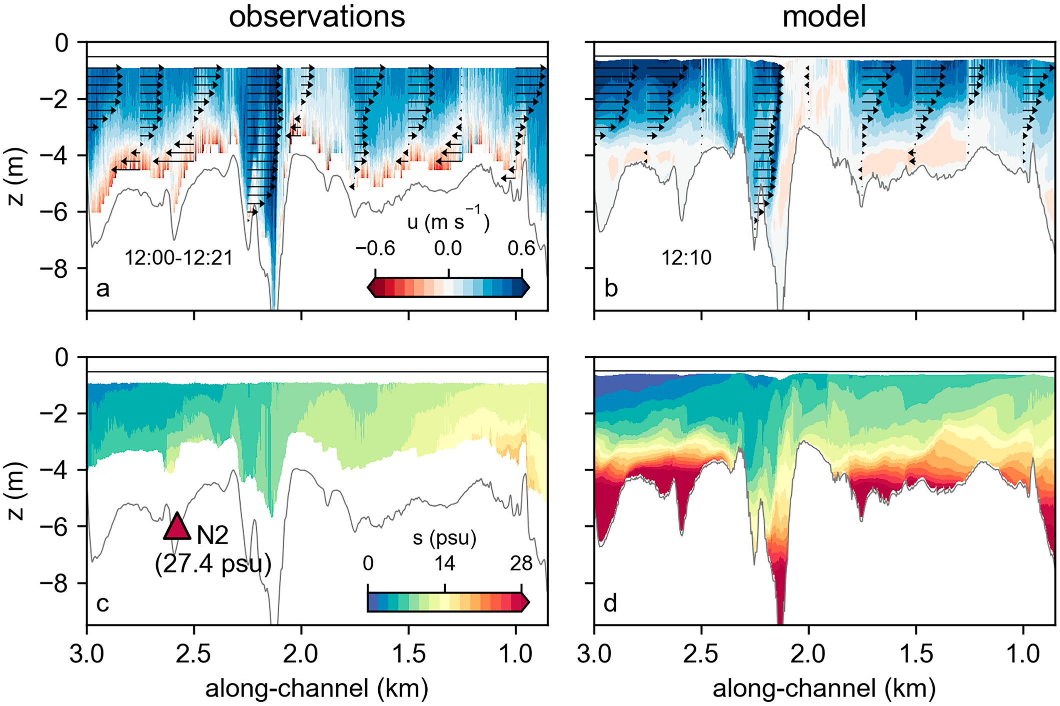

FIG. 4. Tidal straining along the channel during ebb tide on 29 Oct. (a) Streamwise velocity from shipboard ADCP measurements. (b) Streamwise velocity from model output. (c) Salinity profile from towed CTD measurements, with the bottom salinity at the N2 mooring shown by the triangle. (d) Salinity from model output.

at locations N1–N4 and upward-looking AquaDopp profilers (Nortek) at N1, N2, and N3. A comparison of the observations at the N2 mooring with the model over the simulation period is shown in Fig. 2. As shown in Figs. 2b and 2c, the tides and streamwise velocity were well represented by the model. Figures 2d and 2e indicate that stratification and the along-channel salinity gradient, which are particularly important to the dispersive salt flux, were also well represented by the model. Stratification at N2 was slightly greater in the model than in observations, which could contribute to stronger vertical shear dispersion. Nevertheless, the model performed well in capturing the tidal variation of the local salinity structure.

In addition to the moorings, shipboard surveys were conducted with a Signature 1000 (Nortek) acoustic Doppler current profile (ADCP) and a towed array of fast-sampling CTD sensors, similar to the configuration of Simpson et al. (2022). The surveys were conducted both along and across the estuary to measure velocity and salinity profiles. The ADCP velocity measurements had a resolution of approximately 0.2–0.5 m horizontally and 0.3 m vertically, while the towed array salinity measurements had a resolution of approximately 0.1–0.2 m horizontally and 0.5–1.5 m vertically [see Garcia (2022) for full details]. During select days of shipboard surveys, aerial images were obtained using a Da Jiang Innovations (DJI) Phantom 4 drone. These images were georeferenced using fixed landmarks in the images and their coordinates obtained from Google Earth. Observations from the shipboard surveys and aerial images were used to compare with the spatial structure of velocity and salinity produced by the numerical model during spring tide (7 October) and neap tide (29 October) conditions.

During spring tide conditions on 7 October, aerial imagery of flood tide (Fig. 3a) revealed a v-shaped tidal intrusion front (Simpson and Nunes 1981) near the apex of the channel bend near the N2 mooring. The frontal features of this region were evident not only by the surface foam at convergent locations along the front but also the distinct color differences between the water on either side of the front. Shipboard measurements of salinity indicated that lighter green colors corresponded to saltier water while darker blue colors were fresher. This distinct spatial structure was also indicated in the modeled surface salinity (Fig. 3b), which indicated a salinity difference of more than 20 psu across the sharp frontal features. The velocity structures in both the shipboard ADCP surveys (Fig. 3c) and model output (Fig. 3d) indicated a distinct lateral structure in which regions of strong surface currents were separated from relatively stagnant, recirculating currents. The velocity field is strongly tied to the local topography, with faster currents generally corresponding to deeper parts of the channel and regions near channel constrictions. Note that the shipboard measurements took about 40 min to complete, during which time the frontal structure advanced landward due to the strong tidal currents in this region; therefore, there are some differences between the observed and modeled velocities landward of the channel bend apex.

For the high flow, neap tide conditions on 29 October, both observations and model output (Figs. 4a,b) indicated a strongly vertically sheared velocity profile consistent with a two-layer flow in which the bottom layer was close to zero or reversed, i.e., in the flood direction. While the towed array salinity measurements did not capture the full vertical salinity variation due to sampling limitations (Fig. 4c), the bottom N2 mooring salinity was nearly oceanic, consistent with the modeled salinity (Fig. 4d), which indicated a high salinity bottom layer separated from the relatively fresh surface layer by a sharp pycnocline.

d. *Theoretical framework*

1) SUBTIDAL SALT BALANCE

To obtain an equation for the salt budget of an estuary, we begin by integrating the tidally averaged 1D salt equation from a location far enough upriver such that salinity and salt flux are both zero, $x \to -\infty$, to the cross section at an along-channel location x:

$$\frac{\partial}{\partial t}\int_{-\infty}^{x}\left\langle \iint_A s\, dA \right\rangle dx = \frac{\partial M_s}{\partial t} = -\left\langle \iint_A us\, dA \right\rangle \bigg|_x, \tag{1}$$

where angle brackets represent the tidal averaging, s is the salinity, u is the streamwise velocity, A is the cross-sectional area, and M_s is the tidally averaged mass of salt upstream of x (Banas et al. 2004; Lerczak et al. 2006). This equation describes the balance between the time rate of change of the salt content landward of a cross section and the subtidal (tidally averaged) salt flux at that cross section.

The subtidal salt flux on the right-hand side of (1) can be separated into multiple terms, each representing a distinct salt flux mechanism, by decomposing velocity and salinity into multiple components following a series of spatial and temporal averaging (Fischer 1972; Dyer 1974; Hughes and Rattray 1980; Winterwerp 1983; Dronkers and van de Kreeke 1986; Lerczak et al. 2006). Here, following the method as described by Dronkers and van de Kreeke (1986), we decompose velocity and salinity each into three components: 1) cross section and tidally averaged, 2) cross section averaged and tidally varying, and 3) cross sectionally and tidally varying. For example, the salinity components are defined as

$$s_0 = \langle \overline{s} \rangle, \tag{2}$$

$$s_1 = \overline{s} - s_0, \tag{3}$$

$$s' = s - s_1 - s_0, \tag{4}$$

where angle brackets represent the tidal averaging and overbars are the cross-sectional averages, e.g., $\overline{s} = A^{-1}\iint s\, dA$. Here, s_0 is the tidal mean of the cross-section averaged salinity; s_1 is the tidally varying component of the cross-section averaged salinity; and s' is the remaining component, which is the tidally varying deviation from the cross-sectional mean salinity. Note that $s' = s - \overline{s}$, and thus, $\overline{s}' = 0$. The velocity is decomposed in an identical manner. However, to account for the Stokes transport, we also consider the volume transport, $Q = \overline{u}A$, which is decomposed into two terms:

$$Q_0 = \langle Q \rangle, \tag{5}$$

$$Q_1 = Q - Q_0. \tag{6}$$

Here, the first term, Q_0, is the tidally averaged volume transport, which is equivalent to the river discharge, Q_f, at steady state. The second term, Q_1, represents the tidal volume transport. With these definitions, the subtidal salt flux becomes

$$\begin{aligned} F_s &= \left\langle \iint_A (u_0 + u_1 + u')(s_0 + s_1 + s')dA \right\rangle, \\ &= Q_0 s_0 + \langle Q_1 s_1 \rangle + \left\langle \iint_A u's'\, dA \right\rangle, \\ &= F_0 + F_1 + F_2. \end{aligned} \tag{7}$$

Hence, the subtidal salt flux F_s is separated into three distinct terms. The first term, F_0, is the steady advective salt flux due to the river outflow. The second term, F_1, is the nonlocal dispersive salt flux (to be evaluated further in the following section) resulting from the temporal correlation between the tidal volume transport and the tidally varying, cross-section averaged salinity. The final term, F_2, is the local dispersive salt flux resulting from the tidally averaged value of the salt flux due to spatial correlations of velocity and salinity over the cross section. At a steady state when $F_s = 0$, the salt flux due to the river outflow, F_0, must be balanced by the sum of the dispersive salt fluxes, $F_1 + F_2$.

2) NONLOCAL DISPERSIVE SALT FLUX

To provide a physical interpretation of the nonlocal dispersive salt flux, F_1, we use the quasi-Lagrangian moving plane analysis of Dronkers and van de Kreeke (1986). They considered the salt flux through a plane with its tidally varying position defined such that a constant volume of water is maintained between the moving plane and a fixed cross-sectional upstream (landward) of the moving plane where the volume transport is equal to the river discharge, Q_f. Thus, by volume conservation, the volume transport through the moving plane must be equal to Q_f. Assuming the tidal variation of river discharge is small, i.e., $\langle Q_f \rangle \approx Q_f$, then the subtidal salt flux through the moving plane is given by

$$\tilde{F}_s \approx \tilde{Q}_0 \tilde{s}_0 + \left\langle \iint_{\tilde{A}} \tilde{u}'\tilde{s}'\, d\tilde{A} \right\rangle = \tilde{F}_0 + \tilde{F}_2, \tag{8}$$

where tildes denote the variables in the moving plane and subscripts are defined the same as in the fixed cross section. In the moving plane, the temporal correlation term $\tilde{F}_1 \approx 0$ because $\tilde{Q}_1 \approx 0$, and as a result, the steady advective salt flux due to the river outflow, $\tilde{F}_0$, is entirely balanced by the local dispersive salt flux due to spatial correlations of velocity and salinity, $\tilde{F}_2$.

To relate the quasi-Lagrangian salt flux with the Eulerian salt flux, we note that for any fixed cross section with tidally averaged salinity s_0, there exists a moving plane with the same tidally averaged salinity, $\tilde{s}_0$. Under steady-state conditions, $F_s = \tilde{F}_s = 0$ and $Q_0 \approx \tilde{Q}_0 = Q_f$; therefore, we can equate the dispersive salt fluxes in a fixed plane and its corresponding moving plane to obtain

$$F_1 \approx \tilde{F}_2 - F_2. \tag{9}$$

Thus, the nonlocal dispersive salt flux is equal to the difference between the local dispersive salt flux, i.e., shear dispersion, in a plane that moves with the tides and at a fixed cross section. Significant nonlocal dispersion at a fixed location therefore indicates that dispersive processes occurring elsewhere within a tidal excursion are primarily responsible for driving the landward salt flux at that location. Conversely, a countergradient nonlocal salt flux (e.g., Hunkins 1981) can occur in regions where the local dispersive processes are relatively strong compared to the average of those within a tidal excursion. However, for regions where the dispersive salt flux is relatively uniform over length scales of the tidal excursion—or where the local shear dispersion happens to equal the spatial average—the nonlocal dispersive salt flux will be close to zero.

3) LOCAL DISPERSIVE SALT FLUX

While the moving plane analysis of the nonlocal dispersive salt flux provides insight into where dispersion is—or is not—occurring, the mechanisms of dispersion ultimately responsible for driving the landward salt flux can only be determined by the analysis of the spatial correlation salt flux term, $F = \iint_A u's'\,dA$. We will refer to this tidally varying term as the dispersive salt flux, and we note that its tidal average value is the local dispersive salt flux. The dispersive salt flux can be further decomposed to separate between modes of dispersion. Here, in addition to distinguishing between the salt flux due to lateral and vertical shear dispersion, we define an additional salt flux resulting from the mean velocity and salinity differences between distinct regions of a cross section (Fig. 5). This differentiation is made to account for the salt flux associated with the nearly stagnant water that fills the marsh platform at high tide, which represents a form of lateral shear dispersion that is different from the processes occurring within the main channel. A general form for any number of discrete regions defined over a cross section is provided in the appendix.

First, we separate a cross section with area A into two regions corresponding to the channel and the marsh with areas A_c and A_m, respectively, such that $A = A_c + A_m$. Then, we define spatial mean and spatially varying values with respect to those regions. For example, in the channel, we define

$$\overline{s}_c = \frac{1}{A_c}\iint_{A_c} s\,dA, \tag{10}$$

$$s'_c = s - \overline{s}_c, \tag{11}$$

where $\overline{s}_c$ is the mean salinity of the channel and s'_c is the spatially varying deviation of salinity from the mean value in the channel. The velocity components $\overline{u}_c$, u'_c are defined in the same way, as are the variables corresponding to the marsh: $\overline{s}_m$, s'_m, $\overline{u}_m$, u'_m. Thus, the dispersive salt flux can be separated into

$$\begin{aligned} F &= \iint_{A_c} u's'\,dA + \iint_{A_m} u's'\,dA, \\ &= \iint_{A_c} u'_c s'_c\,dA + \iint_{A_m} u'_m s'_m\,dA \\ &\quad + [(\overline{u}_c - \overline{u})(\overline{s}_c - \overline{s})A_c + (\overline{u}_m - \overline{u})(\overline{s}_m - \overline{s})A_m], \\ &= F_c + F_m + F_t, \end{aligned} \tag{12}$$

where F_c is the salt flux due to shear dispersion in the channel, F_m is the salt flux due to shear dispersion over the marsh, and F_t is the salt flux due to the mean velocity and salinity difference between the channel and marsh. Note that the tidally averaged value of F is equal to either F_2 or $\tilde{F}_2$, depending on whether it is analyzed in the Eulerian or moving plane, respectively.

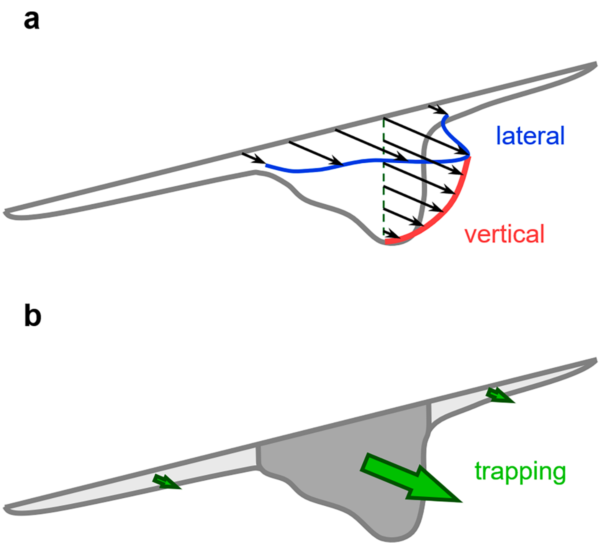

FIG. 5. Schematic of the different contributions to the dispersive salt flux due to spatial correlations of velocity and salinity at a cross section. (a) The dispersive salt flux within the channel is separated into contributions from lateral (blue) and vertical (red) shear dispersion. (b) The dispersive salt flux associated with trapping results from the difference between the mean velocity and salinity in distinct regions of the cross section, A, separated here into the narrow, deep channel, A_c (dark gray), and wide, shallow marsh, A_m (light gray).

Here, we refer to the last term as the "trapping" salt flux, as it represents the salt flux associated with the effects of lateral dead zones or "traps", such as side embayments, shallow marshes, and shoals (Schijf and Schonfeld 1953; Okubo 1973; Fischer et al. 1979). Note that in an Eulerian analysis, if only the salt flux through the main channel region is considered as is often done for field measurements, then the tidally averaged component of the trapping salt flux associated with the channel, $(\overline{u}_c - \overline{u})(\overline{s}_c - \overline{s})A_c$, would contribute to the nonlocal dispersive salt flux rather than the local dispersive salt flux because all of the variables contributing to the trapping term are spatially uniform over the channel region of the cross section. For analyses considering only the limits of the channel region of the cross section, this is consistent with the definition of nonlocal dispersion in an Eulerian reference frame because the trapping salt flux is not caused by local shear dispersion occurring within the channel of a fixed transect.

The dispersive salt flux within either the channel or marsh can be further separated into contributions from lateral and vertical shear dispersion. For example, within the channel, we define

$$s'_{c,l} = \frac{1}{H}\int_H s'_c\,dz, \tag{13}$$

$$s'_{c,v} = s' - s'_{c,l}, \tag{14}$$

where z is the vertical coordinate and H is the water depth. The first term, $s'_{c,l}$, is the depth-averaged component which varies over the cross-channel coordinate y. The second term, $s'_{c,v}$, is the remaining component and includes all vertical variations. The velocity variation u'_c is decomposed in the same manner. Using these definitions, we can separate F_c into its lateral and vertical components:

$$F_{c,l} = \int_{B_c} u'_{c,l}s'_{c,l}H\,dy, \tag{15}$$

$$F_{c,v} = \iint_{A_c} u'_{c,v}s'_{c,v}\,dA, \tag{16}$$

where B_c is the width of the channel. The same decomposition can also be applied in the marsh region, though for this study, the dispersive salt flux due to shear dispersion on the marsh is generally found to be much smaller than the contributions from either trapping or shear dispersion in the channel. Thus, in this paper, the dispersive salt flux in the marsh is not further separated into its lateral and vertical shear components.

We note that the local dispersive salt flux could also be further decomposed into contributions from steady and oscillatory shear dispersion by tidally averaging the spatially varying components of velocity and salinity (Dronkers and van de Kreeke 1986; Lerczak et al. 2006; MacCready and Banas 2012). However, in short estuaries like the North River where tidal variations of velocity and salinity are large, the designation of a steady, spatially varying velocity or salinity field has little physical significance (Imasato 1983). Therefore, in our analysis, we choose not to distinguish between the steady and tidal contributions to shear dispersion and focus instead on the different types of spatial contributions.

4) CALCULATION OF SALT FLUXES

The salt flux terms for the Eulerian and quasi-Lagrangian analyses were calculated from the model output at 10-min intervals over transects spanning the full model width at each u face of the model grid, which was generally aligned with the primary flow direction (Fig. 1). Note that in a highly frontal system like the North River, it is important to calculate the moving plane using high temporal resolution to resolve the spatiotemporally varying velocity and salinity fields. We defined the marsh region of the model domain to include grid cells above an elevation of 0.2 m, in addition to any grid cells located in the tributary channels. Thus, the channel region was defined to include both the main channel and intertidal shoals of the North River.

To calculate the salt fluxes through the moving planes, the position of each moving plane needed to be defined. First, the total volume upstream of each fixed transect, $V(x, t)$, was calculated for every time step of the model output. Then, at the initial time step t_0, an individual moving plane was defined from the volume upstream of each fixed transect of the model grid. Afterward, the tidally varying position of each moving plane was determined for the following time steps based on the location where the upstream volume at that time was equal to the upstream volume of the moving plane at the initial time step. For example, the position of a tidally varying moving plane $X(t)$, which starts at the position $X(t_0) = x$, is defined at each time step based on the maintenance of a constant upstream volume such that $V[X(t), t] = V(x, t_0)$. In practice, the position of each moving plane at each time step was interpolated using a piecewise linear 1D function, $[V(x, t), x]$, evaluated at sample points corresponding to the volumes at the initial time step, $[V(x, t_0)]$.

Once the positions of the moving planes were determined, the instantaneous cross-section averaged salinity ($\bar{s}$) and dispersive salt flux ($F = F_c + F_m + F_t$) were then interpolated onto their locations at each time step. Tidally averaged salinities and salt fluxes were then calculated using a 24-24-25 Godin (1972) filter for the individual planes, each of which was defined by the constant volume maintained between it and the river boundary. For comparison with the fixed Eulerian transects, the subtidal salt flux through a moving plane at each time was matched to a corresponding fixed location where the tidally averaged salinity was the same, i.e., $\tilde{s}_0(X, t) = s_0(x, t)$.

3. Results

a. Along-channel salt flux variation

First, we examine the composition of the Eulerian salt flux, including both local and nonlocal dispersion as described in (7), along the channel for different river and tidal forcing conditions (Fig. 6). Notably, the local dispersive salt flux alone, i.e., the spatial correlation $u's'$ in the fixed Eulerian transects, is insufficient to explain the total landward salt flux in the channel. Instead, a substantial portion of the salt flux is attributed to nonlocal dispersion (the temporal correlation between the cross-section averaged velocity and salinity), which relates to shear dispersion that occurs elsewhere in the estuary within a tidal excursion (Dronkers and van de Kreeke 1986).

The magnitude of the total landward Eulerian flux increased during high river flow periods (e.g., Fig. 6d), and it generally balanced with Q_0s_0, the seaward advective salt flux driven by river flow. The relative importance of local and nonlocal dispersion varied with tidal forcing. Nonlocal dispersive salt flux dominated during spring tides, contributing over 70% of the total landward salt flux, while it accounted for a smaller fraction of the total salt flux when tides were weaker.

Spatially, the total Eulerian flux increased toward the mouth of the estuary, corresponding to the along-estuary shape of the salinity distribution. However, the local dispersive flux was highly variable along the channel, and the local peaks were likely

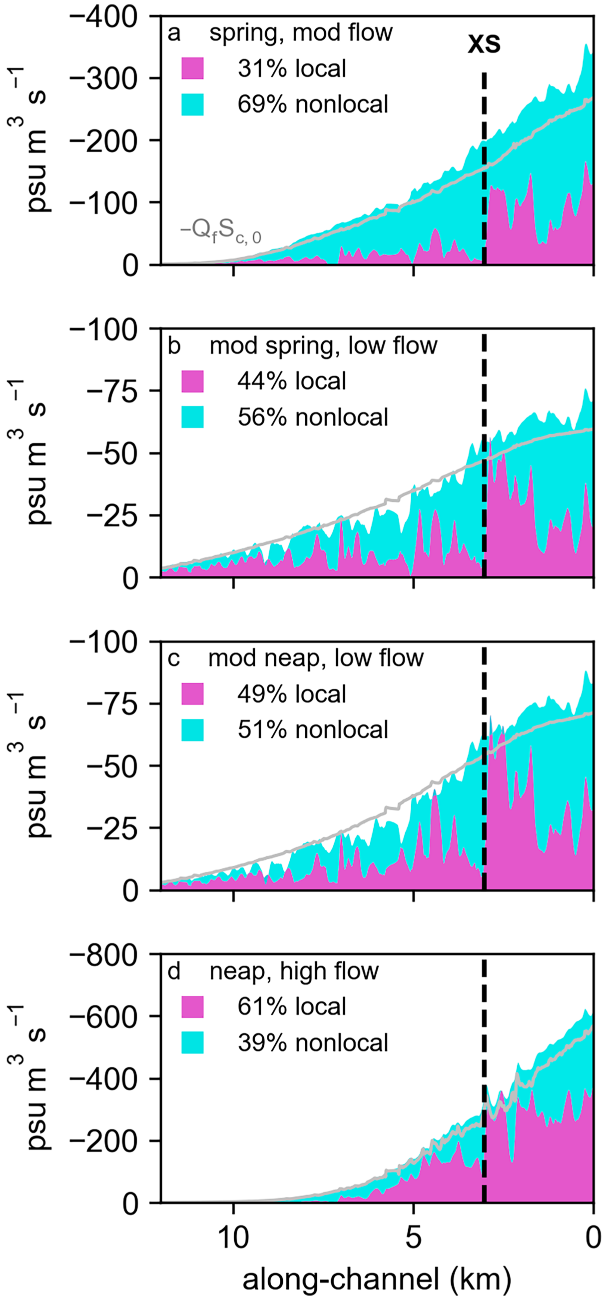

FIG. 6. Composition of the Eulerian salt flux along the channel under different estuarine forcing conditions. (a) Spring tide, moderate flow on 7 Oct. (b) Moderate spring tide, low flow on 21 Oct. (c) Moderate neap tide, low flow on 14 Oct. (d) Neap tide, high flow on 29 Oct. The gray line represents the seaward salt flux due to the river. The difference between the gray line and the sum of the dispersive salt fluxes is the storage term. The along-channel location of the fixed cross section at 3 km is indicated by the black dashed line.

associated with topographic features in the North River estuary. In the subsequent sections, we will focus on a representative cross section located at 3 km from the mouth (shown in Fig. 1 and indicated by the vertical dashed line in Fig. 6) to compare the analysis of salt fluxes using both Eulerian and quasi-Lagrangian reference frames.

b. *Eulerian salt fluxes*

In this section, we examine the Eulerian salt balance through the main channel at a transect located at 3 km (Fig. 7), where a constriction separates the lower channel–shoal region near the mouth from the upper narrow channel region (Fig. 1). For the Eulerian approach, we considered only the main channel region of the cross section because the marsh region at this defined transect was disconnected from the main channel, which made evaluation of Eulerian salt fluxes through the full transect less amenable to physical interpretation. Additionally, we note that the main channel region of the cross section is the portion that could be compared directly with field observations.

In the channel, the advective salt flux due to the river was balanced by the sum of nonlocal and local dispersive salt fluxes, such that the sum of the three salt flux terms was almost exactly equal to the storage term, except for around 27 October during the sea level setup and setdown (Fig. 7b). During that short period, the sum of salt fluxes exceeded the storage terms in first the landward (gain salt) direction and then the seaward (lose salt) direction, which suggests that some storage of salt occurred outside the channel region in the marsh. In general, peaks in the nonlocal and local dispersive salt fluxes usually occurred about 1 day after the peaks in the river salt flux, representing the relatively short response time of the estuary to high discharge events (Kranenburg 1986). While short-term variations in the total salt flux through the main channel were apparent, the average value over the simulation period was close to zero, indicating a long-term balance over the record.

At this location, nonlocal dispersion was the primary driver of landward salt flux (Fig. 7b). Local dispersion only contributed significantly to the landward salt flux during the neap tide, high flow conditions which occurred on 29 October. The dominance of the nonlocal term indicates that dispersive processes outside of this fixed channel cross section must account for the remaining dispersive salt fluxes. Note that when only the salt fluxes through the main channel region are considered, as is the case here, the nonlocal dispersive salt flux corresponds not only to dispersive processes elsewhere along the channel but also to tidal trapping due to differences in the mean velocity and salinity of the main channel compared to the marsh and side channels. To explain the variation of the nonlocal dispersive salt fluxes, we next examine the salt fluxes using the quasi-Lagrangian moving plane reference frame.

c. *Moving plane salt fluxes*

Here, we examine the subtidal salt fluxes through the moving plane with the same tidally averaged salinity as the fixed cross section at 3 km (Fig. 8). Note that when using the moving plane approach, we must consider the salt fluxes through the entire transects, i.e., the full width of the model domain (see Fig. 1), to maintain the volume balance and boundary by which the moving planes are defined. While the orientation of a transect spanning the full model width at a single location may be disconnected or misaligned with the main channel flow direction, the tidally

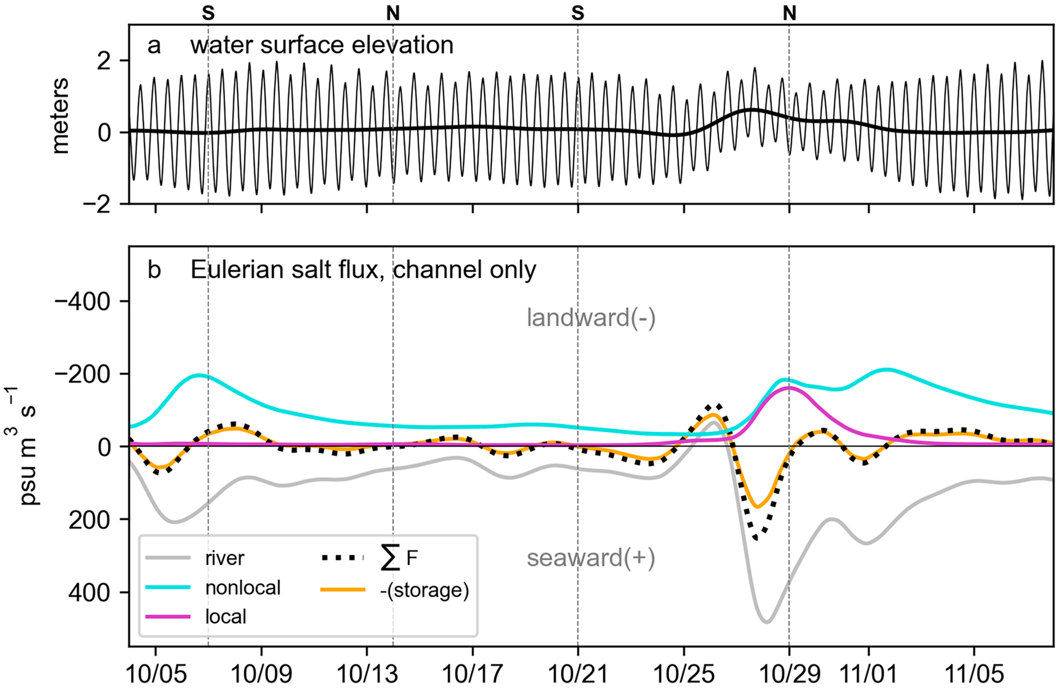

FIG. 7. Eulerian salt flux decomposition in the channel of the cross section located at 3 km. (a) Water level (thin black line) with the tidally averaged value (thick black line) shown to highlight the sea level setup on 27 Oct. (b) Salt flux decomposition calculated from the model using the grid points in the channel region of the cross section. The individual salt flux terms are the river outflow (gray), nonlocal dispersive salt flux (cyan), and local dispersive salt flux (magenta). The subtidal salt balance is shown by the sum of the three salt flux terms (black dotted line) and the storage term (orange). The vertical dotted lines indicate the time periods shown in Figs. 6 and 15.

moving plane reference effectively applies a spatial filter to the salt flux which averages over multiple transect orientations that are, on average, both connected and aligned with the main channel flow.

The tidally varying position of the moving plane corresponding to the 3-km cross section ranged from an along-channel position of about 1–8 km during spring tides and only 1.5–4 km during the smallest neap tides (Fig. 8a). Although the moving plane crossed the transect at 3 km during each tidal cycle, its mean spatial position was not centered around the fixed location. This is due to the smaller cross-sectional areas and correspondingly larger cross-section averaged velocities landward of the 3-km transect as compared to those seaward.

In the moving plane reference system, the seaward salt flux due to the river outflow was balanced entirely by the local dispersive salt flux, i.e., the tidally averaged contribution from spatial correlations of velocity and salinity (Fig. 8b). Compared to the traditional Eulerian reference frame, the quasi-Lagrangian moving plane approach of Dronkers and van de Kreeke (1986) therefore provides a more natural coordinate system for analyzing dispersion contributing to the salt balance at this location because all the landward salt fluxes can be directly accounted for based on the local, tidally varying structure of velocity and salinity over a tidal excursion.

In the following sections, we demonstrate how the moving plane framework can be utilized to identify the distinct mechanisms responsible for producing the landward salt flux under spring and neap tidal conditions.

d. *Spring tide*

1) LOCAL DISPERSIVE SALT FLUX THROUGH THE MOVING PLANE

During the spring tide on 7 October, the position of the moving plane corresponding to the fixed cross section (3 km) ranged from 1.5 to 8.5 km from the mouth (Figs. 9a,b). High tide occurred about 2 h before the moving plane reaches its maximum landward extent at the end of flood tide, which indicates the partially progressive phasing of the tide in the upper reaches of the estuary; however, low tide (LT) was nearly coincident with the moving plane reaching its maximum seaward extent at the end of ebb tide, which indicates nearly standing wave tidal conditions in the lower reach of the estuary (Friedrichs and Aubrey 1994).

The magnitude and composition of the instantaneous dispersive salt flux varied significantly over the tidal cycle (Fig. 9c). Within the channel, the dispersive salt flux due to shear dispersion—both vertical and lateral—was largest during peak flood tide as the moving plane passed between 2 and 3 km (Fig. 9b). Notably, this was the only time and location during which there was significant shear dispersion within the channel. While shear dispersion on the marsh itself contributed very

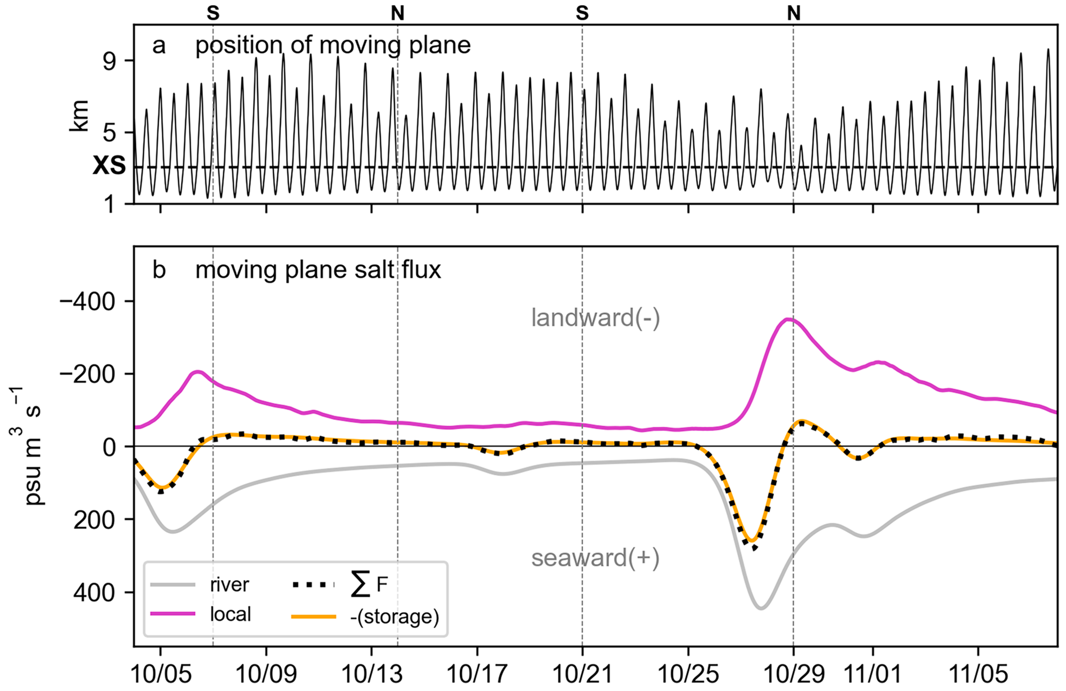

FIG. 8. Moving plane analysis of salt fluxes corresponding to the cross section located at 3 km. (a) Position of the moving plane, which is determined at each model time step based on the individual plane having the same tidally averaged salinity as the fixed cross section at 3 km. (b) Salt flux decomposition through the moving plane. The individual salt flux terms are the river outflow (gray) and local dispersive salt flux (magenta). The subtidal salt balance is shown by the sum of the two salt flux terms (black dotted line) and the storage term (orange). The vertical dotted lines indicate the time periods shown in Figs. 6 and 15.

little to the landward salt flux, trapping due to the mean velocity and salinity differences between the channel and the marsh was a large contributor to the salt balance. The dispersive salt flux due to trapping peaked during distinct periods of the tide as the moving plane passed through different regions. When the plane passed through the region between 1 and 2 km around low tide, the trapping salt flux was seaward (countergradient) during flood tide but landward (downgradient) during ebb. However, when the plane passed through the region between 5 and 6 km around high tide, the trapping salt flux was landward during flood tide but seaward during ebb. Although the trapping salt flux associated with these two regions (1–2 and 5–6 km) alternated between landward and seaward over the tidal cycle, their tidally averaged contributions were net landward. Furthermore, the tidal average sum of all the tidally varying salt flux terms in Fig. 9c was equal to the local dispersive salt flux on 7 October (Fig. 8).

In the following subsections, we will examine the velocity and salinity distributions at cross sections corresponding to the location of the moving plane during these periods of peak dispersive salt flux.

2) LATERAL FLOW SEPARATION

Within the channel, shear dispersion was notably enhanced as the moving plane passed through the region of complex topography between 2 and 3 km during flood tide (Fig. 9). Figure 10 demonstrates the spatial structure of the dispersive salt flux due to the spatial correlation between velocity and salinity, which were strongly correlated over the cross section due to the region of fast and salty water being separated by a shear layer from the slow and freshwater in the flow separation zone (Figs. 10a,c). However, we note the presence of a lobe of countergradient salt flux, which results from the anticorrelation between velocity and salinity in the stratified region of the jet. This is because the upstream (seaward) salinity distribution did not have time to adjust to the velocity shear, so there remains a low-salinity anomaly in the center of the channel where the flood velocities are maximal. As the flood progresses, differential advection would cause the fastest-moving water to have higher salinities throughout the estuary, resulting in more uniform, downgradient salt flux.

3) TRAPPING

In this section, we examine a cross section from the region between 5 and 6 km and demonstrate how the dispersive salt flux due to trapping results from the local structure of velocity and salinity, which differs significantly between the channel and the marsh.

During flood tide (Fig. 11) as the marsh filled, the main channel had much stronger (landward) currents and higher salinity than the marsh region of the cross section. This lateral salinity structure was the result of the straining of the along-channel salinity gradient into the lateral direction by differential advection. The combination of the local velocity and salinity structure led

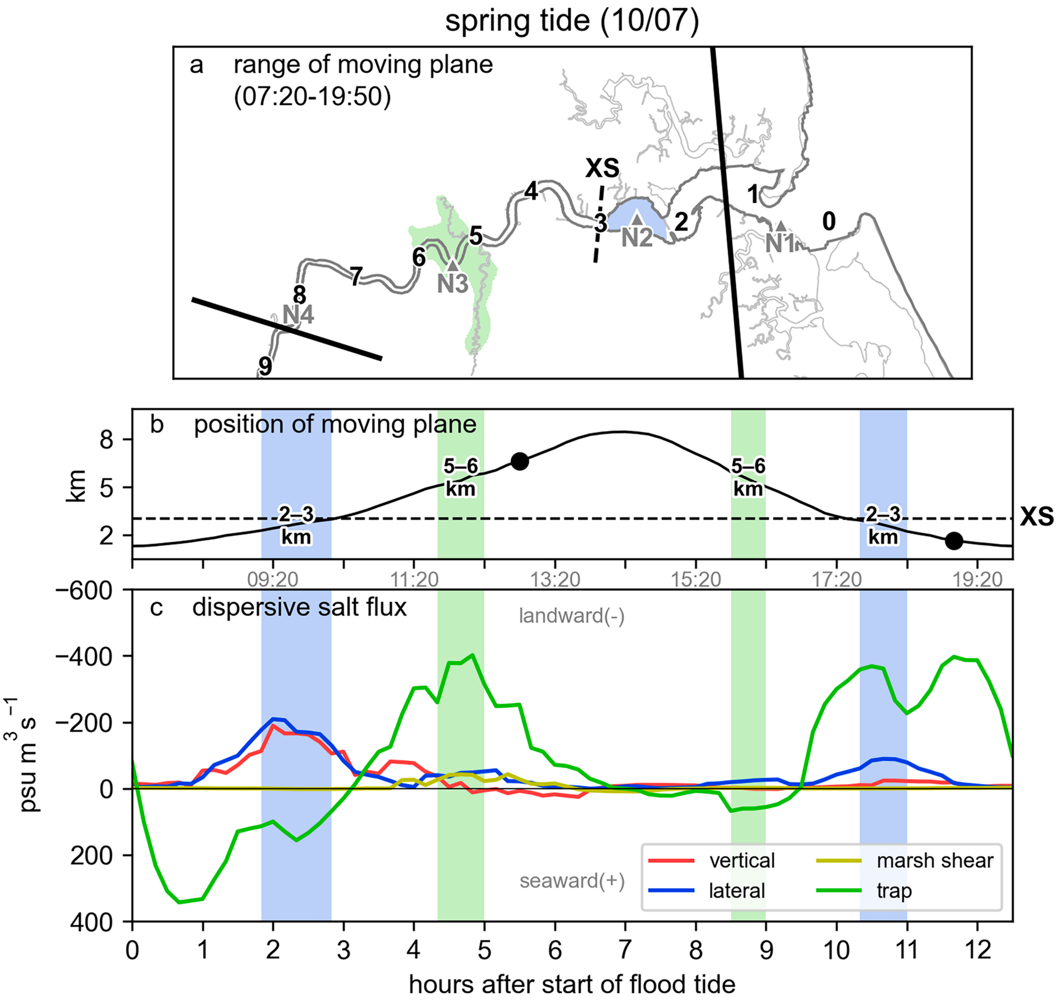

FIG. 9. Dispersive salt flux through the moving plane corresponding to the fixed cross section at 3 km during spring tidal conditions on 7 Oct. (a) Map showing range of the moving plane, with blue shading in the region from 2 to 3 km and green shading in the region from 5 to 6 km. (b) Time series of tidally varying position of the moving plane (solid) compared to the fixed transect (dashed). The times for HT and LT are indicated by the black circles. (c) Time series of dispersive salt flux contributions through the moving plane due to vertical shear dispersion in the channel (red), lateral shear dispersion in the channel (blue), total shear dispersion on the marsh (gold), and trapping (green). In (b) and (c), the color shading corresponds to the times during which the moving plane passes through the blue (2–3 km) and green (5–6 km) regions highlighted in (a).

to a landward salt flux due to saltier water preferentially entering through the fast-flowing channel, while fresher water stayed behind in the low velocities regions over the marsh (Fig. 11c).

During ebb tide, the (seaward) currents were stronger in the main channel than in the marsh region (Fig. 12). However, the main channel remained saltier than the marsh due to the lateral structure left over from differential advection during the preceding flood tide, similar to observations in Delaware Bay by Geyer et al. (2020). Thus, the resulting dispersive salt flux due to trapping was seaward during the ebb tide, corresponding to higher salinity water exiting the estuary through the fast-flowing channel region. This period of countergradient salt flux indicates that some of the dispersion accomplished by trapping during flood tide was reversible. As noted in previous studies (Fischer et al. 1979; Young et al. 1982), reversible oscillatory dispersion can occur if the mixing time scale which “locks in” the dispersion is comparable to or longer than the tidal period. Nonetheless, the net salt flux due to trapping was downgradient when averaged over the tidal cycle, consistent with the description of trapping by Okubo (1971).

We note that the opposite flood–ebb pattern of landward and seaward salt flux due to trapping was observed for low tide when the moving plane passed through the region between 1 and 2 km near the mouth. Examination of the velocity and salinity structure in this region (not shown here) indicated that the streamwise currents were stronger in the main channel than in the marsh and side channels, while the salinity of the main channel was lower. This difference in relative salinity of the

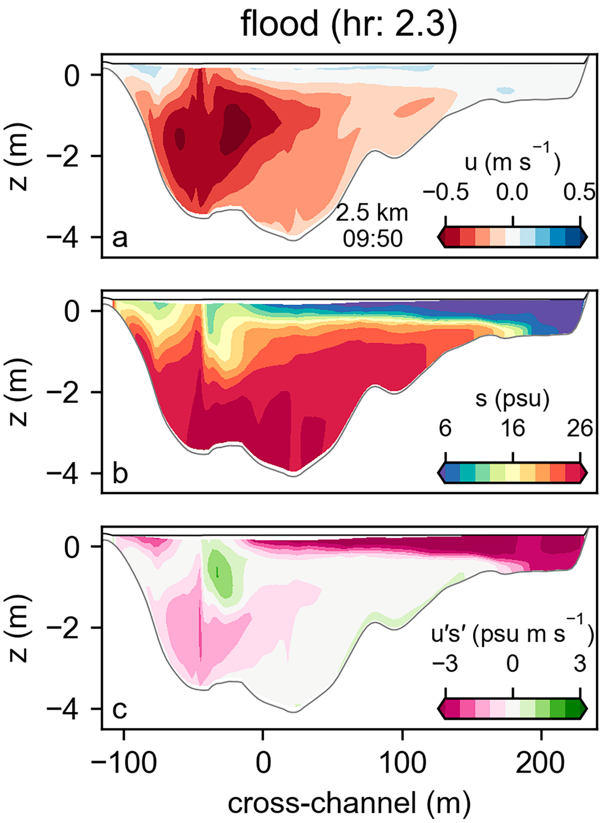

FIG. 10. Flood tide (a) velocity, (b) salinity, and (c) dispersive salt flux through channel cross section at 2.2 km at 0950 EST 7 Oct, 2.3 h after start of flood tide.

main channel compared to the marsh may be due to differences in the marsh topography and tidal phasing in the intertidal region near the mouth as compared to the upper-channel region.

e. Neap tide

1) LOCAL DISPERSIVE SALT FLUX THROUGH THE MOVING PLANE

The tidal excursion of the moving plane corresponding to the fixed cross section (3 km) during the neap tide, high river flow conditions on 29 October ranged from only 1.5 to 4.2 km, about half the distance traveled during spring tide (Figs. 13a,b). The durations of flood tide and ebb tide were nearly equal, with slack tides occurring about 40 min after high tide and around the same time as low tide. Note that compared to the spring tide previously described, the along-channel salinity gradient was much larger due to the higher river discharge. Similarly to the previous section, the tidal average sum of all the tidally varying salt flux terms in Fig. 13c was equal to the local dispersive salt flux in Fig. 8 on 29 October.

In contrast to the spring tide conditions, vertical shear dispersion in the channel contributed most significantly to the dispersive salt flux throughout the tidal cycle, indicating a persistent structure of vertical shear and stratification in the moving plane reference frame (Fig. 13c). As the moving plane passed the region from 2 to 3 km during flood tide, lateral shear dispersion was landward, but during ebb tide, lateral shear dispersion was seaward. This suggests reversible shear dispersion due to incomplete mixing (Bowden 1965; Fischer et al. 1979), i.e., the lateral salinity structure produced by differential advection during flood tide was effectively undone when the tide reversed through the ebb. Trapping was small during flood tide but increased during portions of the ebb tide. Given that the marsh was not inundated under these conditions, this dispersive salt flux must have been the result of trapping in the side channels.

2) TIDAL STRAINING

Baroclinically driven shear enhanced by tidal straining (Simpson et al. 1990) during ebb tide was the primary mechanism of dispersion in the main channel during neap tide, high flow

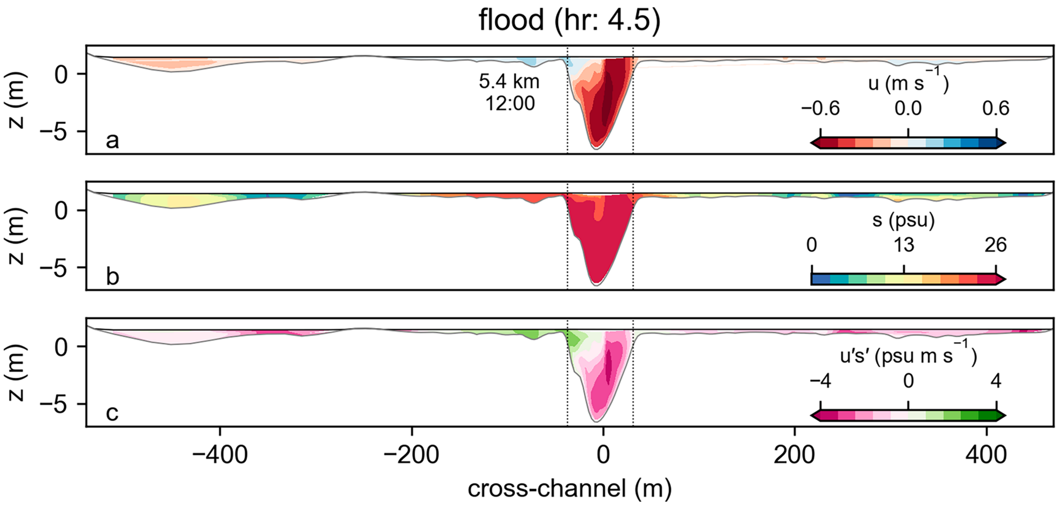

FIG. 11. Flood tide (a) velocity, (b), salinity, and (c) dispersive salt flux through marsh channel cross section at 5.4 km at 1200 EST 7 Oct, 4.5 h after start of flood tide.

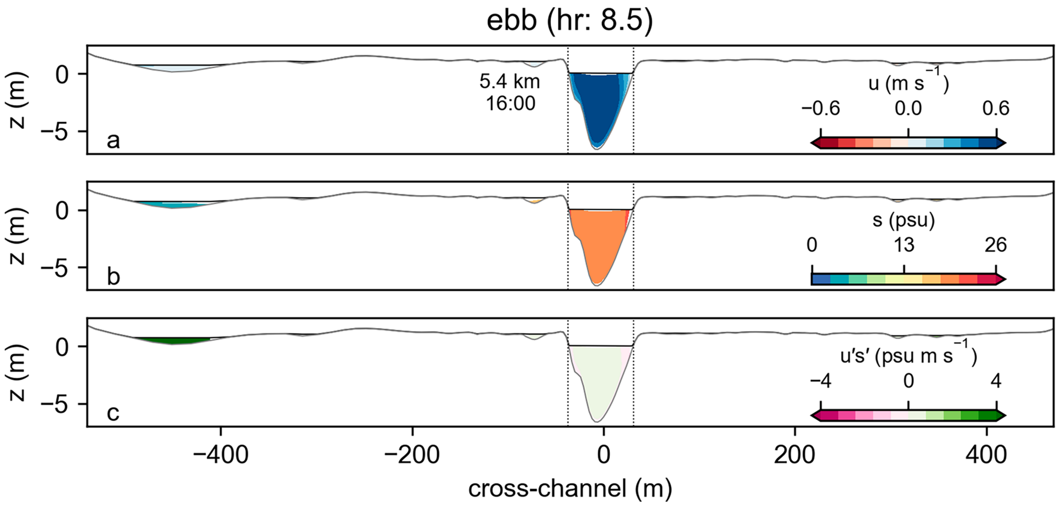

FIG. 12. Ebb tide (a) velocity, (b), salinity, and (c) dispersive salt flux through marsh channel cross section at 5.4 km at 1600 EST 7 Oct, 8.5 h after start of flood tide.

conditions on 29 October (Fig. 14). The combination of vertically sheared velocity and salinity stratification produced a landward salt flux because the relatively freshwater at the surface was preferentially transported downstream, while the saltier bottom water was left behind. Despite stratification being nearly uniform across the channel at this time, the velocities were laterally sheared with stronger currents generally located in the deeper midsection of the channel; this spatial pattern resulted in the lobes of countergradient salt flux on the lateral fringes of the channel, which correspond to the seaward lateral dispersive salt flux during ebb tide in Fig. 13c.

4. Discussion

a. Mechanisms of dispersion

When analyzed using the moving plane framework, the landward salt flux along the length of the estuary can be entirely separated into its contributions from different modes of dispersion, which vary depending on the estuarine forcing conditions (Fig. 15).

Trapping accounted for up to half the landward salt flux during spring tide (Fig. 15a) but only about one-quarter during neap tides (Figs. 15c,d). This strong dependence of trapping on the tidal forcing is consistent with analytical parameterizations of tidal trapping (Schijf and Schonfeld 1953; Okubo 1973; Dronkers 1978; MacVean and Stacey 2011), which are generally of the form

$$K_{\mathrm{trap}} = \alpha \frac{rU_t^2}{\omega}, \tag{17}$$

where K_{trap} is an effective, tidally averaged dispersion coefficient, α is a coefficient, r is the ratio of trap volume to channel volume, U_t is the tidal velocity amplitude, and ω is the tidal frequency. For the spring tide conditions, $U_t \approx 0.5$ m s^{-1}, $r \approx 0.3$, $K_{\mathrm{trap}} \approx 64$ m^2 s^{-1}, and $\omega = 1.4 \times 10^{-4}$ s^{-1}, resulting in a coefficient of about $\alpha \approx 0.1$, generally consistent with previous estimates (Geyer and Signell 1992). Equation (17) demonstrates how larger tides can increase the tidal trapping dispersion in two ways: 1) by increasing the tidal velocity amplitude, U_t, and 2) by increasing the ratio r by filling the traps—in this case, the marsh and side channels—with a greater volume of water.

Within the channel, the primary mode of shear dispersion transitioned from lateral to vertical as the tidal forcing decreases. The landward salt flux due to lateral shear was 2–3 times bigger than vertical shear during spring tides (Figs. 15a,b). During intermediate neap tides (Fig. 15c), the landward salt flux due to lateral shear was about twice as much as vertical shear. As river flow increased and tidal forcing decreased to neap conditions, the landward salt flux due to lateral shear decreased to about one-quarter of the salt flux due to vertical shear (Fig. 15d). This transition suggests that spring tides have stronger lateral flow separation and turbulent mixing with faster tidal currents, whereas neap tides have weaker—or completely suppressed—flow separation and weaker turbulent mixing (and thus stronger stratification). This spring–neap transition in the dominant mechanisms of shear dispersion has been previously characterized using an estuarine Richardson number (Fischer 1972; Garcia and Geyer 2023).

Note that during intermediate tidal forcing conditions (Figs. 15b,c), the relative contributions from different modes of local dispersive salt flux vary spatially along the channel. While trapping and lateral shear dispersion dominate downstream of the channel constriction at 3 km in the channel–shoal region near the mouth, vertical shear dispersion becomes more important upstream of the channel constriction at 3 km in the narrow channel region. These patterns reflect the topographic influence on the dominant modes of dispersion: more side channels and larger marsh area increase trapping near the mouth, while wider main channel cross sections combined with local constrictions in the channel–shoal region enable stronger lateral shear dispersion as compared to the more uniform, narrower channel upstream.

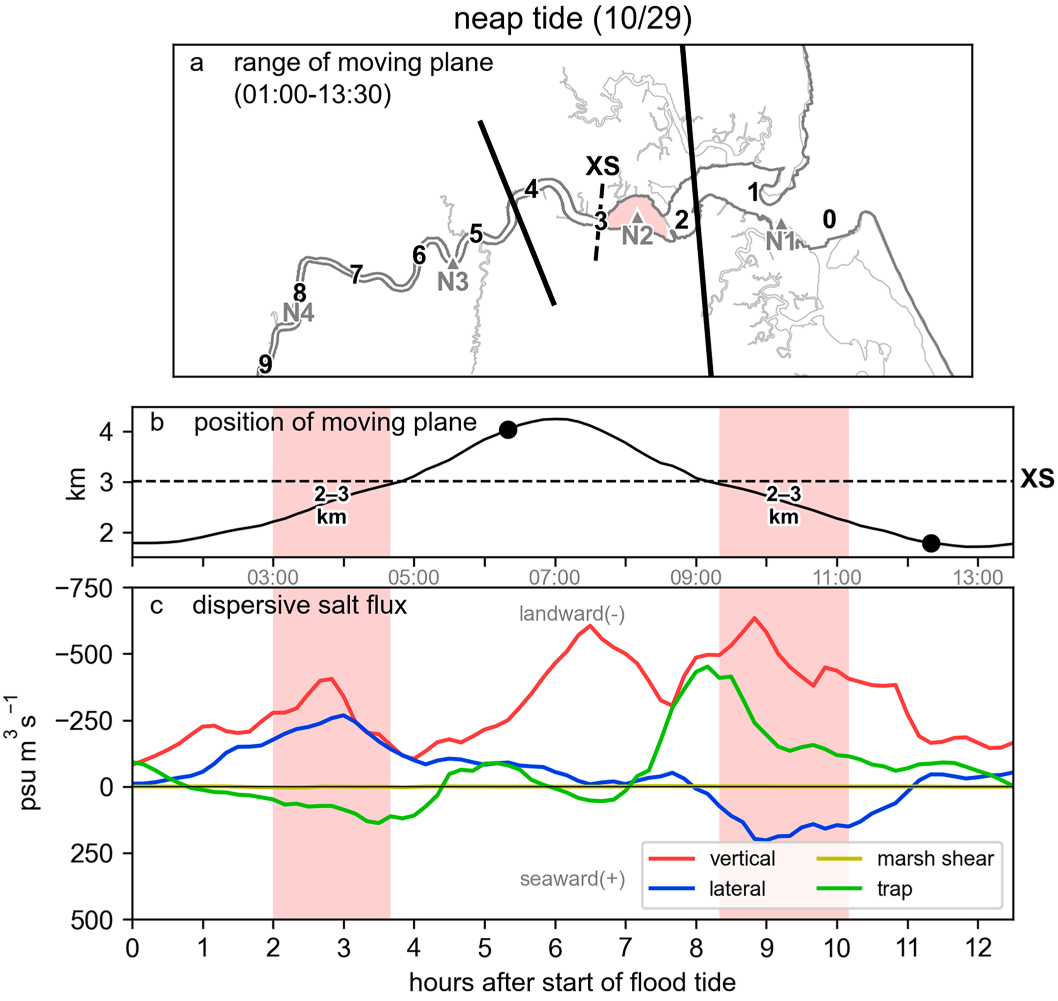

FIG. 13. Dispersive salt flux through the moving plane corresponding to the fixed cross section at 3 km during neap tidal conditions on 29 Oct. (a) Map showing range of the moving plane, with red shading in the region from 2 to 3 km. (b) Time series of tidally varying position of the moving plane (solid) compared to the fixed transect (dashed). The times for HT and LT are indicated by the black circles. (c) Time series of dispersive salt flux contributions through the moving plane due to vertical shear dispersion in the channel (red), lateral shear dispersion in the channel (blue), total shear dispersion on the marsh (gold), and trapping (green). In (b) and (c), the color shading corresponds to the times during which the moving plane passes through the red (2–3 km) region highlighted in (a).

b. Application of the moving plane framework

As demonstrated above, the moving plane approach to analyzing salt fluxes enables diagnosing the mechanisms of dispersion in estuaries, especially those with complex, variable topography. A drawback of this approach, however, is that it requires high spatial and temporal resolution of data at multiple cross sections to be applied accurately; as a result, quantitative application of this method is likely limited to modeling studies. Nevertheless, the insights gained from the quasi-Lagrangian reference frame can be used to understand how local regions that are highly dispersive can impact the overall salt balance within a tidal excursion.

Even if the "moving plane" analysis is not performed, the division of the Eulerian salt flux into local and nonlocal components does provide insights into the mechanisms of salt flux that emerge from the theory of Dronkers and van de Kreeke (1986). For any location where the nonlocal salt flux dominates, there must be regions upstream or downstream of that cross section where local salt fluxes are more intense. Conversely, if the nonlocal salt flux is countergradient, then the local salt flux at that cross section must be anomalously large. Evaluating the variation of local and nonlocal salt transport along an estuary will reveal those "hotspots" of shear dispersion that contribute to the nonlocal transport in the adjacent sections of the estuary; for example, in Fig. 6, the local dispersive salt flux was relatively higher seaward of the cross section at 3 km, corresponding to the shear dispersion in the frontal region.

It is worthwhile to compare the moving plane framework not only to the traditional Eulerian approach for analyzing salt fluxes but also to the total exchange flow (TEF) (MacCready 2011).

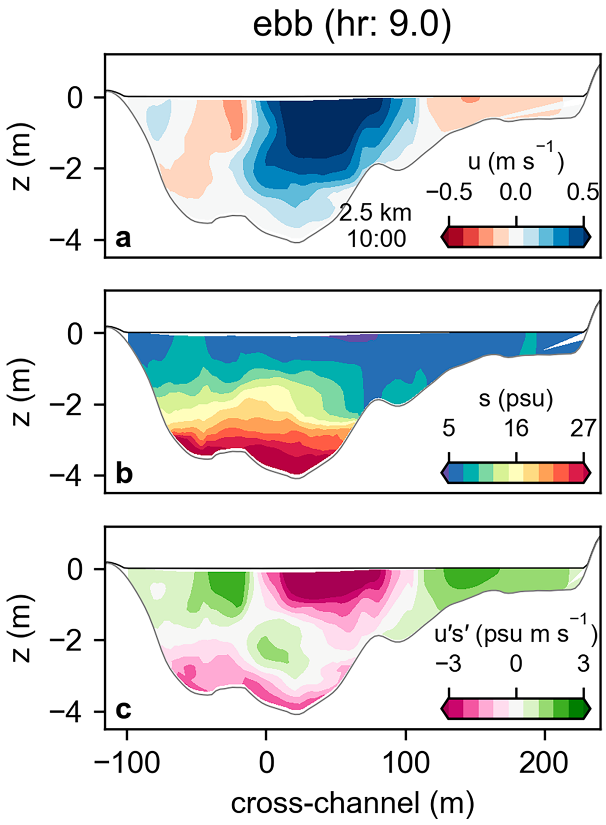

FIG. 14. Ebb tide (a) velocity, (b) salinity, and (c) dispersive salt flux through channel cross section at 2.2 km at 1000 EST 29 Oct, 9 h after start of flood tide.

Like the moving plane method, TEF is a quasi-Lagrangian approach for analyzing salt flux (Wang et al. 2015). A major advantage of TEF is that it provides a bulk characterization of all the dispersive mechanisms relevant to a cross section. Furthermore, TEF can be calculated at a single fixed cross section, even using a limited number of sample points, as shown by Lemagie et al. (2022). However, TEF does not provide an explicit linkage between the subtidal salt flux and the tidally varying, local salt flux, and TEF is typically regarded as representing a form of the classical vertically sheared estuarine circulation. Thus, for estuaries in which estuarine circulation is not the primary driver of salt flux, such as tidally dominated estuaries where the salinity intrusion is similar to the tidal excursion length (Chen et al. 2012), the moving plane approach utilized here may be better suited to understanding the dependencies of salt fluxes on estuarine forcing conditions.

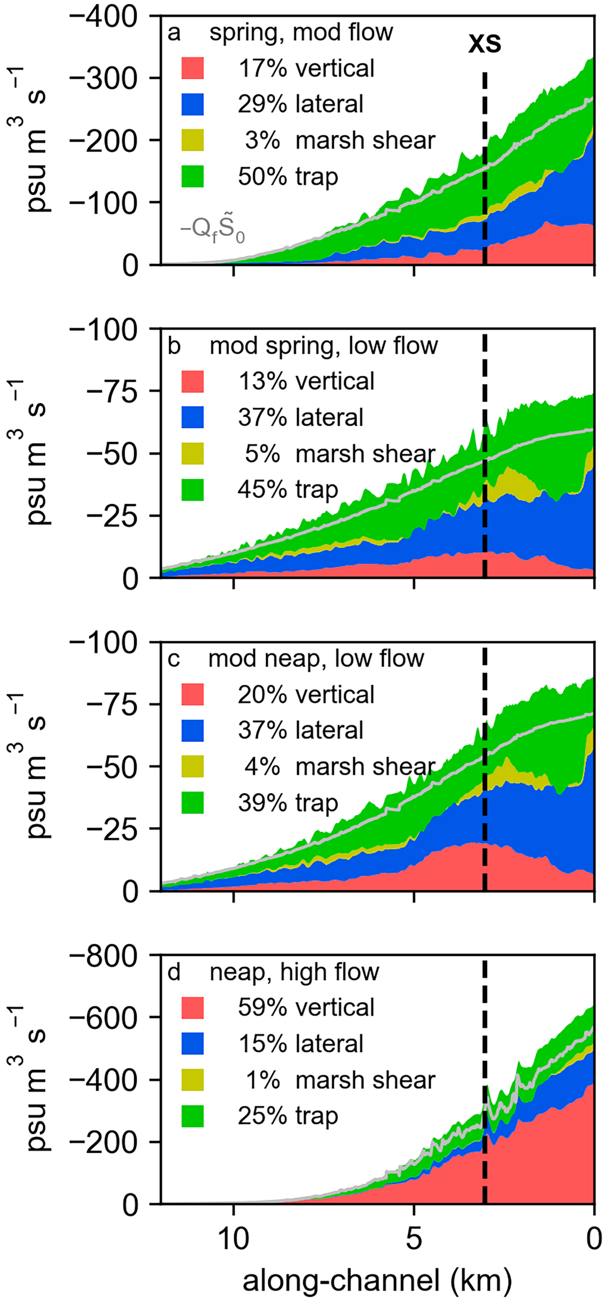

FIG. 15. Composition of the local dispersive salt flux along the channel under different estuarine forcing conditions. (a) Spring tide, moderate flow on 7 Oct. (b) Moderate spring tide, low flow on 21 Oct. (c) Moderate neap tide, low flow on 14 Oct. (d) Neap tide, high flow on 29 Oct. The light gray line represents the magnitude of the seaward salt flux due to the river. The difference between the light gray line and the sum of the dispersive salt fluxes is the storage term (i.e., unsteadiness). The along-channel location of the fixed cross section at 3 km is indicated by the black dashed line.

5. Conclusions

The North River is a tidal salt marsh estuary in which nonlocal salt fluxes—the tidal correlation between the cross-section averaged velocity and salinity—contribute significantly to the salt balance. Based on the theory of Dronkers and van de Kreeke (1986), the nonlocal salt flux in the Eulerian reference frame is equal to the difference between the shear dispersion through a reference frame that moves with the tides and the shear dispersion at a fixed cross section. In the moving plane reference, all salt fluxes are driven by spatial correlations between velocity and salinity over the cross section, i.e., shear dispersion.

Here, we distinguished between different forms of shear dispersion not only by decomposing the cross-sectionally varying velocity and salinity into their laterally and vertical varying components but also by separating the cross-sectional area into two distinct regions: the main channel and the marsh. In this way, the instantaneous dispersive salt flux can be separated into contributions from lateral and vertical shear dispersion, as well as trapping—the salt flux resulting from differences between the mean velocity and salinity of the main channel compared to the lateral storage areas, that is, the marsh and side channels.

We applied the moving plane framework and salt flux decomposition to a realistic model of the North River to identify and quantify the primary mechanisms of dispersion contributing to the landward salt flux under different estuarine forcing conditions. By following the path of the moving plane and examining the tidal variation of different components of the tidally varying dispersive salt flux, we identified regions and forcing conditions under which various topographic features impacted the dominant mode of dispersion. During spring tides, the dispersion due to trapping of water on the marsh and side channels accounted for up to half of the landward salt flux, while during neap tides, dispersion due to trapping accounted for only about one-quarter of the total. Within the channel, the landward salt flux during spring tides was primarily driven by lateral shear dispersion, which was locally enhanced in regions of flow separation due to constrictions and sharp channel curvature. During neap tides, vertical shear dispersion in the channel due to tidal straining was the primary driver of the landward salt flux. Although the salt flux due to trapping was large, the local shear dispersion within the marsh and side channels was negligible compared to the total landward salt flux throughout the estuary.

The moving plane framework provides a useful approach for diagnosing the mechanisms responsible for maintaining the salt balance in estuaries with large topographic variations occurring at length scales shorter than the tidal excursion. For example, the moving plane framework could be used to quantify the salt flux contributions from trapping in branching channel systems like the Coos estuary (Conroy et al. 2020) or to determine the spatial influence of dispersion around channel modifications in urbanized estuaries, such as the Duwamish River (McKeon et al. 2021). However, direct application of this quasi-Lagrangian method is likely limited to numerical modeling studies due to the need for high spatial and temporal resolution of velocity and salinity at multiple cross sections along the estuary. Nevertheless, the insights gained from this study and the moving plane methodology highlight the important role of topographic features on dispersive processes in tidally dominated estuaries.

Acknowledgments. This project was funded by NSF Awards OCE-1634480 and OCE-2123002. The research presented here is also based upon work supported by the NSF Graduate Research Fellowship under Grant 1122374. The authors thank Jay Sisson, Sean Whelan, Noa Randall, and Salme Cook for field assistance. We also thank two anonymous reviewers for careful reading and thoughtful suggestions, which have improved clarity of the manuscript.

Data availability statement. Model data and field observations supporting this study are available online at https://doi.org/10.5281/zenodo.14073744.

APPENDIX

General Form for the Trapping Dispersive Salt Flux

Here, we provide a general form for the shear and trapping components of the dispersive salt flux based on separation of a cross section into N distinct regions. This type of designation may be useful for transects which span across topographic features such as branching channels, shoals, or marshes.

For a cross section whose total area is A, any number of nonoverlapping regions (N) may be defined such that

$$A = \sum_{i=1}^{N} A_i, \tag{A1}$$

where A_i is the area of the cross section responding to the region i. Then, we define the spatial mean and spatially varying values with respect to each region. For salinity, we define in each region

$$\overline{s}_i = \frac{1}{A_i}\iint_{A_i} s\, dA, \tag{A2}$$

$$s'_i = s - \overline{s}_i, \tag{A3}$$

where $\overline{s}_i$ is the mean salinity over the i region and s'_i is the spatially varying deviation of salinity from the mean value in the i region. The velocity components, $\overline{u}_i$, u'_i, are defined in the same manner as the salinity components.

The salt flux due to trapping, F_t, is distinguished from the salt flux due to shear dispersion within each region, F_i, by evaluating the dispersive salt flux area integral separately over the area of each region and then substituting $s' = s - \overline{s} = (\overline{s}_i + s'_i) - \overline{s}$ and $u' = u - \overline{u} = (\overline{u}_i + u'_i) - \overline{u}$ to obtain

$$\begin{aligned} F &= \sum_{i}^{N} \iint_{A_i} u's'\, dA, \\ &= \sum_{i}^{N} \iint_{A_i} u'_i s'_i\, dA + \sum_{i}^{N} (\overline{u}_i - \overline{u})(\overline{s}_i - \overline{s}) A_i, \\ &= \sum_{i}^{N} F_i + F_t. \end{aligned} \tag{A4}$$

REFERENCES

Banas, N. S., B. M. Hickey, P. MacCready, and J. A. Newton, 2004: Dynamics of Willapa Bay, Washington: A highly unsteady, partially mixed estuary. *J. Phys. Oceanogr.*, **34**, 2413–2427, https://doi.org/10.1175/JPO2637.1.

Bo, T., D. K. Ralston, W. M. Kranenburg, W. R. Geyer, and P. Traykovski, 2021: High and variable drag in a sinuous estuary with intermittent stratification. *J. Geophys. Res. Oceans*, **126**, e2021JC017327, https://doi.org/10.1029/2021JC017327.

——, ——, and W. R. Geyer, 2023: Sources of drag in estuarine meanders: Momentum redistribution, bottom stress enhancement, and bend-scale form drag. *J. Phys. Oceanogr.*, **53**, 1629–1650, https://doi.org/10.1175/JPO-D-22-0211.1.

——, ——, A. M. P. Garcia, and W. R. Geyer, 2024: Tidal intrusion fronts, surface convergence, and mixing in an estuary with complex topography. *J. Phys. Oceanogr.*, **54**, 653–677, https://doi.org/10.1175/JPO-D-23-0131.1.

Bowden, K. F., 1965: Horizontal mixing in the sea due to a shearing current. *J. Fluid Mech.*, **21**, 83–95, https://doi.org/10.1017/S0022112065000058.

Chapman, D. C., 1985: Numerical treatment of cross-shelf open boundaries in a barotropic coastal ocean model. *J. Phys. Oceanogr.*, **15**, 1060–1075, https://doi.org/10.1175/1520-0485(1985)015<1060:NTOCSO>2.0.CO;2.

Chatwin, P. C., 1976: Some remarks on the maintenance of the salinity distribution in estuaries. *Estuarine Coastal Mar. Sci.*, **4**, 555–566, https://doi.org/10.1016/0302-3524(76)90030-X.

Chen, S.-N., W. R. Geyer, D. K. Ralston, and J. A. Lerczak, 2012: Estuarine exchange flow quantified with isohaline coordinates: Contrasting long and short estuaries. *J. Phys. Oceanogr.*, **42**, 748–763, https://doi.org/10.1175/JPO-D-11-086.1.

Conroy, T., D. A. Sutherland, and D. K. Ralston, 2020: Estuarine exchange flow variability in a seasonal, segmented estuary. *J. Phys. Oceanogr.*, **50**, 595–613, https://doi.org/10.1175/JPO-D-19-0108.1.

Dronkers, J., 1978: Longitudinal dispersion in shallow well-mixed estuaries. *Proc. 16th Int. Conf. on Coastal Engineering*, Hamburg, Germany, American Society of Civil Engineers, 2761–2777, https://doi.org/10.1061/9780872621909.171.

——, and J. van de Kreeke, 1986: Experimental determination of salt intrusion mechanisms in the Volkerak estuary. *Neth. J. Sea Res.*, **20** (1), 1–19, https://doi.org/10.1016/0077-7579(86)90056-6.

Dyer, K. R., 1974: The salt balance in stratified estuaries. *Estuarine Coastal Mar. Sci.*, **2**, 273–281, https://doi.org/10.1016/0302-3524(74)90017-6.

Fischer, H. B., 1972: Mass transport mechanisms in partially stratified estuaries. *J. Fluid Mech.*, **53**, 671–687, https://doi.org/10.1017/S0022112072000412.

Flather, R. A., 1976: A tidal model of the north-west European continental shelf. *Mem. Soc. Roy. Sci. Liege*, **10**, 141–164.

Fischer, H. B., E. J. List, R. C. Y. Koh, J. Imberger, and N. H. Brooks, 1979: *Mixing in Inland and Coastal Waters*. Academic Press, 483 pp.

Friedrichs, C. T., and D. G. Aubrey, 1994: Tidal propagation in strongly convergent channels. *J. Geophys. Res.*, **99**, 3321–3336, https://doi.org/10.1029/93JC03219.

Garcia, A. M. P., 2022: Mechanisms of tidal dispersion in a salt marsh estuary. Ph.D. thesis, Massachusetts Institute of Technology and Woods Hole Oceanographic Institution, 144 pp., https://dspace.mit.edu/handle/1721.1/147458.

——, and W. R. Geyer, 2023: Tidal dispersion in short estuaries. *J. Geophys. Res. Oceans*, **128**, e2022JC018883, https://doi.org/10.1029/2022JC018883.

——, ——, and N. Randall, 2022: Exchange flows in tributary creeks enhance dispersion by tidal trapping. *Estuaries Coasts*, **45**, 363–381, https://doi.org/10.1007/s12237-021-00969-4.

Geyer, W. R., and R. P. Signell, 1992: A reassessment of the role of tidal dispersion in estuaries and bays. *Estuaries*, **15**, 97–108, https://doi.org/10.2307/1352684.

——, D. K. Ralston, and J.-L. Chen, 2020: Mechanisms of exchange flow in an estuary with a narrow, deep channel and wide, shallow shoals. *J. Geophys. Res. Oceans*, **125**, e2020JC016092, https://doi.org/10.1029/2020JC016092.

Godin, G., 1972: *The Analysis of Tides*. University of Toronto Press, 264 pp.

Haidvogel, D. B., and Coauthors, 2008: Ocean forecasting in terrain-following coordinates: Formulation and skill assessment of the Regional Ocean Modeling System. *J. Comput. Phys.*, **227**, 3595–3624, https://doi.org/10.1016/j.jcp.2007.06.016.

Hansen, D. V., and M. Rattray Jr., 1965: Gravitational circulation in straits and estuaries. *J. Mar. Res.*, **23**, 104–122.

Hughes, F. W., and M. Rattray Jr., 1980: Salt flux and mixing in the Columbia River estuary. *Estuarine Coastal Mar. Sci.*, **10**, 479–493, https://doi.org/10.1016/S0302-3524(80)80070-3.

Hunkins, K., 1981: Salt dispersion in the Hudson estuary. *J. Phys. Oceanogr.*, **11**, 729–738, https://doi.org/10.1175/1520-0485(1981)011<0729:SDITHE>2.0.CO;2.

Imasato, N., 1983: What is tide-induced residual current? *J. Phys. Oceanogr.*, **13**, 1307–1317, https://doi.org/10.1175/1520-0485(1983)013<1307:WITIRC>2.0.CO;2.

Kranenburg, C., 1986: A time scale for long-term salt intrusion in well-mixed estuaries. *J. Phys. Oceanogr.*, **16**, 1329–1331, https://doi.org/10.1175/1520-0485(1986)016<1329:ATSFLT>2.0.CO;2.

Kranenburg, W. M., W. R. Geyer, A. M. P. Garcia, and D. K. Ralston, 2019: Reversed lateral circulation in a sharp estuarine bend with weak stratification. *J. Phys. Oceanogr.*, **49**, 1619–1637, https://doi.org/10.1175/JPO-D-18-0175.1.

Lemagie, E. P., S. N. Giddings, P. MacCready, C. Seaton, and X. Wu, 2022: Measuring estuarine total exchange flow from discrete observations. *J. Geophys. Res. Oceans*, **127**, e2022JC018960, https://doi.org/10.1029/2022JC018960.

Lerczak, J. A., W. R. Geyer, and R. J. Chant, 2006: Mechanisms driving the time-dependent salt flux in a partially stratified estuary. *J. Phys. Oceanogr.*, **36**, 2296–2311, https://doi.org/10.1175/JPO2959.1.

Luettich, R. A., Jr., J. J. Westerink, and N. W. Scheffner, 1992: ADCIRC: An advanced three-dimensional circulation model for shelves, coasts, and estuaries. Report 1, Theory and methodology of ADCIRC-2DD1 and ADCIRC-3DL. DRP Tech. Rep. DRP-92-6, 143 pp., https://apps.dtic.mil/sti/tr/pdf/ADA261608.pdf.

MacCready, P., 2011: Calculating estuarine exchange flow using isohaline coordinates. *J. Phys. Oceanogr.*, **41**, 1116–1124, https://doi.org/10.1175/2011JPO4517.1.

——, and N. S. Banas, 2012: Residual circulation, mixing, and dispersion. *Treatise Estuarine Coastal Sci.*, **2**, 75–89, https://doi.org/10.1016/B978-0-12-374711-2.00205-9.

MacVean, L. J., and M. T. Stacey, 2011: Estuarine dispersion from tidal trapping: A new analytical framework. *Estuaries Coasts*, **34**, 45–59, https://doi.org/10.1007/s12237-010-9298-x.

McKeon, M. A., A. R. Horner-Devine, and S. N. Giddings, 2021: Seasonal changes in structure and dynamics in an urbanized salt wedge estuary. *Estuaries Coasts*, **44**, 589–607, https://doi.org/10.1007/s12237-020-00788-z.

Okubo, A., 1971: Oceanic diffusion diagrams. *Deep-Sea Res. Oceanogr. Abstr.*, **18**, 789–802, https://doi.org/10.1016/0011-7471(71)90046-5.

——, 1973: Effect of shoreline irregularities on streamwise dispersion in estuaries and other embayments. *Neth. J. Sea Res.*, **6**, 213–224, https://doi.org/10.1016/0077-7579(73)90014-8.

Pritchard, D. W., 1952: Salinity distribution and circulation in the Chesapeake Bay estuarine system. *J. Mar. Res.*, **11**, 106–123.

Schijf, J. B., and J. C. Schonfeld, 1953: Theoretical considerations on the motion of salt and fresh water. *Proc. Minnesota Int. Hydraulics Convention*, Minneapolis, MN, IAHR, 321–333, https://repository.tudelft.nl/file/File_a7f0dd0b-13bd-4999-990e-20b539ee011f.

Shchepetkin, A. F., and J. C. McWilliams, 2005: The Regional Oceanic Modeling System (ROMS): A split-explicit, free-surface, topography-following-coordinate oceanic model. *Ocean Modell.*, **9**, 347–404, https://doi.org/10.1016/j.ocemod.2004.08.002.

Simpson, A. J., F. Shi, J. T. Jurisa, D. A. Honegger, T.-J. Hsu, and M. C. Haller, 2022: Observations and modeling of a buoyant plume exiting into a tidal cross-flow and exhibiting along-front instabilities. *J. Geophys. Res. Oceans*, **127**, e2021JC017799, https://doi.org/10.1029/2021JC017799.

Simpson, J. H., and R. A. Nunes, 1981: The tidal intrusion front: An estuarine convergence zone. *Estuarine Coastal Shelf Sci.*, **13**, 257–266, https://doi.org/10.1016/S0302-3524(81)80024-2.

——, J. Brown, J. Matthews, and G. Allen, 1990: Tidal straining, density currents, and stirring in the control of estuarine stratification. *Estuaries*, **13**, 125–132, https://doi.org/10.2307/1351581.

Stommel, H. M., and H. G. Farmer, 1952: *On the Nature of Estuarine Circulation: Part I (Chapters 3 and 4)*. Woods Hole Oceanographic Institution, 172 pp.

Taylor, G. I., 1953, Dispersion of soluble matter in solvent flowing slowly through a tube. *Proc. Roy. Soc.*, **219A**, 186–203, https://doi.org/10.1098/rspa.1953.0139.

——, 1954: The dispersion of matter in turbulent flow through a pipe. *Proc. Roy. Soc.*, **223A**, 446–468, https://doi.org/10.1098/rspa.1954.0130.

Umlauf, L., and H. Burchard, 2003: A generic length-scale equation for geophysical turbulence models. *J. Mar. Res.*, **61**, 235–265, https://doi.org/10.1357/002224003322005087.

Wang, T., W. R. Geyer, P. Engel, W. Jiang, and S. Feng, 2015: Mechanisms of tidal oscillatory salt transport in a partially stratified estuary. *J. Phys. Oceanogr.*, **45**, 2773–2789, https://doi.org/10.1175/JPO-D-15-0031.1.

Warner, J. C., W. R. Geyer, and J. A. Lerczak, 2005a: Numerical modeling of an estuary: A comprehensive skill assessment. *J. Geophys. Res.*, **110**, C05001, https://doi.org/10.1029/2004JC002691.

——, C. R. Sherwood, H. G. Arango, and R. P. Signell, 2005b: Performance of four turbulence closure models implemented using a generic length scale method. *Ocean Modell.*, **8**, 81–113, https://doi.org/10.1016/j.ocemod.2003.12.003.

——, Z. Defne, K. Haas, and H. G. Arango, 2013: A wetting and drying scheme for ROMS. *Comput. Geosci.*, **58**, 54–61, https://doi.org/10.1016/j.cageo.2013.05.004.

Winterwerp, J. C., 1983: Decomposition of the mass transport in narrow estuaries. *Estuarine Coastal Shelf Sci.*, **16**, 627–638, https://doi.org/10.1016/0272-7714(83)90075-6.

Young, W. R., P. B. Rhines, and C. J. R. Garrett, 1982: Shear-flow dispersion, internal waves and horizontal mixing in the ocean. *J. Phys. Oceanogr.*, **12**, 515–527, https://doi.org/10.1175/1520-0485(1982)012<0515:SFDIWA>2.0.CO;2.

Zimmerman, J. T. F., 1986: The tidal whirlpool: A review of horizontal dispersion by tidal and residual currents. *Neth. J. Sea Res.*, **20**, 133–154, https://doi.org/10.1016/0077-7579(86)90037-2.